

Strong Ionospheric Spatial Gradient Events Induced by Signal Propagation Paths Aligned With Equatorial Plasma Bubbles

BRUNO JACOBINI AFFONSO 

Instituto Tecnológico de Aeronáutica, São José dos Campos, Brazil

ALISON MORAES 

Instituto de Aeronáutica e Espaço, São José dos Campos, Brazil

JONAS SOUSASANTOS 

Instituto Tecnológico de Aeronáutica, São José dos Campos, Brazil

LEONARDO MARINI-PEREIRA 

Institute of Airspace Control, São José dos Campos, Brazil

SAM PULLEN 

Stanford University, Stanford, CA USA

Low-latitude ionospheric behavior directly interferes with a wide range of applications dependent on signals and information from

Manuscript received June 29, 2021; revised November 19, 2021 and December 19, 2021; released for publication January 2, 2022. Date of publication January 25, 2022; date of current version August 9, 2022.

DOI No. 10.1109/TAES.2022.3144622

Refereeing of this contribution was handled by S. Khanafseh.

The work of B. J. Affonso was supported by the framework of the INCT GNSS-NavAer Project under Grant CNPq 465648/2014-2 and Grant FAPESP 2017/50115-0. The work of A. Moraes was supported by the CNPq award 314043/2018-7 and the work of J. Sousasantos was supported by the FAPESP under Grant 2018/06158-9. The scintillation monitoring stations deployed in the context of Projects CIGALA/CALIBRA were supported by Grant FP7-GALILEO-2009-GSA and Grant FP7-GALILEO-2011-GSA-1a, as well as of FAPESP under Grant 06/04008-2 and the data was accessed at <http://ismrquerytool.fct.unesp.br/is/> using ISMR Query Tools.

Authors' addresses: Bruno Jacobini Affonso and Jonas Sousasantos are with the Instituto Tecnológico de Aeronáutica, São José dos Campos 12228-900, Brazil, E-mail: (jonasjss@ita.br); Alison Moraes is with Instituto de Aeronáutica e Espaço, São José dos Campos 12228-904, Brazil, E-mail: (aom@ita.br); Leonardo Marini-Pereira is with the Institute of Airspace Control, São José dos Campos 12228-615, Brazil, E-mail: (marinilmp@fab.mil.br); Sam Pullen is with the Department of Aeronautics & Astronautics, Stanford University, Stanford, CA 94305 USA, E-mail: (SPullen@stanford.edu). (*Corresponding author: Bruno Jacobini Affonso.*)

satellites. The most severe and variable events are plasma bubbles and ionospheric scintillation. During plasma bubble events, large and steep plasma density gradients may intersect transionospheric signal from satellites, especially around the equatorial anomaly region. Large ionospheric spatial gradients (or decorrelations) are a critical component of ionospheric threat models for global navigation satellite systems augmentation systems; however, the models cannot assimilate abrupt changes in ionospheric behavior. In this article, an investigation of the relationship between plasma depletions, the occurrence of scintillation, and strong ionospheric spatial decorrelation events was conducted. The results indicate that strong scintillations occur when large gradients are verified. Additionally, the most critical ionospheric spatial gradients were verified mostly under certain conditions: when satellite signals are aligned with the plasma bubble propagation along geomagnetic field lines. Therefore, even though amplitude scintillation may degrade communications, the critical gradient events seem to be related to a particular configuration of satellite signal across the ionosphere. Thus, it is recommended that ionospheric threat models for augmentation systems in low-latitude regions consider this alignment aspect.

I. INTRODUCTION

Global navigation satellite systems (GNSS) are widely used for navigation on different platforms. In aviation, GNSS is commonly the primary navigation sensor used to operate within area navigation and required navigation performance airspace for enroute, terminal maneuvering, and approach flight phases. However, the accuracy, integrity, and availability of standard or "open-service" GNSS provided by constellations such as the global positioning system (GPS) and Galileo do not by themselves support precise operations because of errors in the range measurement from satellites to receivers. Among these errors, the ionospheric delay contributes the largest and most unpredictable errors for a single-frequency user [30].

In order to mitigate these errors, GNSS augmentation systems, such as the space-based augmentation system (SBAS) and the ground-based augmentation system (GBAS) were developed. Both SBAS and GBAS broadcast range measurement corrections to users to improve the accuracy and integrity of the measurements and comply with demanding operational requirements. GBAS provides corrections for the local area surrounding a ground station fielded at an airport, while SBAS has much wider (regional or continental) coverage. GBAS provides more accurate corrections and supports precise landing operations like Category I precision approach.

A GBAS facility works by providing corrections to users (approaching aircraft) along with integrity parameters and the desired approach path. The corrections, which contribute to improving range and position accuracy, are broadcast via a VHF channel, and are computed at the ground facility for all ranging sources in view that pass a series of integrity monitors designed to detect and remove anomalous measurements. The broadcast corrections are estimated considering the line of sight between the ground station and each satellite. Variations on the ionospheric conditions along the line of sight between the user and the same satellite as viewed by the nearby ground facility result in small residual error due to the spatial decorrelation of the ionosphere (and other factors). This error increases with the user's distance to the ground station reference receivers and can be approximately quantified by a linear variation rate that represents the residual error obtained at each linear

unit of separation from the ground station. This variation is a gradient commonly expressed in units of mm/km.

Under nominal conditions, residual errors due to ionospheric decorrelation are bounded by a parameter broadcast by the GBAS ground facility, namely sigma vig (vertical ionospheric gradient), whose value is determined from previous studies of data obtained near the locations where GBAS is to be deployed [12]. However, anomalous and threatening gradients can occur, and a strategy called “geometry screening” must be applied [11]. This method conservatively assumes that the worst gradient (from the point of view of an approaching aircraft) is always occurring. The worst gradients that can occur are defined by an ionospheric threat model. This approach reduces the system’s availability but must be done to fulfill the stringent integrity requirements demanded by a safety-critical application like GBAS [3], [21]. Indeed, efforts have been devoted to methods to detect and alert the occurrence of strong ionospheric gradient events, as reported in [9] and [13]. In mid-latitude regions such as the Contiguous United States (CONUS) and almost all of Europe, the most severe gradients found (e.g., see [31]) still allow an acceptable level of availability after applying geometry screening, even with conservative assumptions. However, in low-latitude regions, the gradients found for the ionospheric threat model in Brazil published by [26] generate impractically low availability levels even when this GBAS threat model is only applied during the vulnerable times of day [26]. The ionospheric environment in low latitudes has also a strong effect on SBAS resulting in low availability, as evidenced by [19].

In this context, it is vital to investigate and characterize ionospheric spatial gradients in low latitudes. Further knowledge about how and when these gradients occur can help avoid conservative approaches and thus improve the potential performance of GBAS in low-latitude regions. The threats of greatest concern for augmentation systems in low latitudes, especially GBAS due to its vulnerability to extreme ionospheric spatial gradients, are so-called equatorial plasma bubbles (EPBs). In fact, the detection of EPBs providing early scintillation alerts is a very important issue in this sense, it is worth mentioning the works of [28] and [37] where strategies are proposed to reduce such vulnerability for the GNSS users.

EPBs rise over the ionospheric equatorial region after the sunset and propagate vertically reaching the ionospheric topside. These structures are believed to be generated by the Rayleigh–Taylor instability, as they are initially driven by bottom-side perturbations that cause the formation of polarized electric fields. As the initial perturbations evolve, the growth rate increases, eventually becoming nonlinear. As the depleted structures reach the topside over the equator, they propagate to off-equator regions because of the large parallel conductivity along the field lines. In low-latitude regions, there is a concentration of plasma around the equator at approximately $\pm 15^\circ$ magnetic latitude, known as the equatorial ionization anomaly (EIA), because of the so-called fountain effect. It should be noticed that, although EPBs have an equatorial origin, the largest gradients caused by these structures will be found over the EIA due to the larger background plasma density in this region.

Moreover, during EPB events, secondary instabilities at several wavelengths are produced, causing the effect known as ionospheric scintillation in radio signals. Strong

ionospheric scintillation environment, which is expected at low latitudes as shown by [17], can lead GPS receivers to lose carrier tracking loop during deep signal fading as discussed in [14] and modeled in [35]. Hence, EPBs degrade communications in at least two ways: by causing scintillation and creating severe and abrupt plasma density gradients along the signal path, leading to spatial decorrelation of ionospheric delay. For simplicity, total electron content (TEC) is often used to evaluate these phenomena. TEC is defined as the integral of the electron density along the signal path (considering a unitary cylinder) and is expressed in units of 10^{16} electrons/m².

Ionospheric spatial decorrelation is an important parameter used in the ionospheric threat models for augmentation systems. The ionospheric threat model for GBAS in the CONUS has an upper bound of 375–425 mm/km [31]. However, due to the low-latitude ionospheric phenomenology described above, models developed for mid-latitude regions generally do not apply to low-latitude regions such as Brazil. Yoon *et al.* [26] observed and verified many ionospheric spatial decorrelation events above the upper bound of the CONUS model over the Brazilian region. The largest of these gradients reached a value of 850.7 mm/km on March 1st, 2014. Harris *et al.* [21] further scrutinized this large gradient and showed that EPBs caused this event. Yoon *et al.* [26] also presented a methodology to validate observed extreme ionospheric spatial gradients induced by EPB events over low-latitude regions. Harris *et al.* [21] presented a case with the largest gradients ever reported, reaching 850.7 mm/km on March 1st, 2014. They scrutinized this large gradient and showed that EPBs caused this event. Over the Asia-Pacific region, Saito *et al.* [34] conducted a study to determine a model for the ionospheric delay gradient for GBAS. In this article, an upper bound of 600 mm/km for the ionospheric threat model was determined and was driven by low-latitude observations within the Asia-Pacific region. Another important work was done by [21] and [35] using a simulation approach to represent a depleted structure and the correspondent gradient in three dimensions and its effects on GBAS operations.

Data provided by GNSS networks have been extensively used to study the effects of ionospheric gradients on GNSS operations. Lee *et al.* [12] estimated typical ionospheric gradients for nominal days in CONUS, determining an upper bound for the standard deviation of the vig. Moraes *et al.* [3] showed that the occurrences of strong scintillation events were concentrated around the magnetic meridian whose large declination (21.4° W) in that region corresponds to an azimuth of $\sim 345^\circ$ and whose magnetic inclination corresponds to an elevation angle of $\sim 37^\circ$. These numbers suggest that strong scintillation events may occur more often when the GPS line of sight is aligned with the EPBs along the geomagnetic field lines. Previously, Saito *et al.* [35] evaluated the influence of alignment using simulation. Their results were very interesting and indicated the need for field validation. Additionally, Yoon *et al.* [23] considered EPB-aligned measurements to explain their results. They worked with a study of case on March 1, 2014. Their alignment assumption does not specify the angle between the elevation and the geomagnetic field inclination as in [3]. Motivated by all these previous articles, the present article deepens the investigation broadening the analysis with several cases of EPB-induced ionospheric gradients under aligned and

nonaligned situations. Also, the alignment condition is specified in the azimuthal and elevation directions (i.e., with relation to the declination and inclination of the geomagnetic field). In addition, the statistical approach considering a wider dataset provides new insights showing the coherence between EPBs-aligned signals, spatial gradients magnitude, and the probability involved in this interrelation. The results covered a considerable range of EPB events supporting the simulations done by [37] and the conclusions suggested by [23]; therefore, the findings in this article are more specific and based on the results of a significant amount of data agreeing with theoretical models and smaller segment of data from previous articles.

The second (and next) section presents a description of the dataset and the methodology used in this article. The third section presents an analysis concerning amplitude scintillation and ionospheric spatial gradients over São José dos Campos, Brazil. The consequences of GPS line of sight alignment with EPB structures are then investigated in detail using the dataset, which contains both amplitude scintillation and severe ionospheric spatial gradients. Final remarks and conclusions are presented in the last section.

II. DATASET AND IONOSPHERIC GRADIENT PROCESSING

In the present article, ionospheric delay gradient analysis was performed using a dataset composed of 16 local nights from November 15 to 30, 2014 (inclusive) collected from GPS satellites with elevation angles above 12°. The assessment considered data from 18:00 to 03:00 local time (LT), which is the time window where EPB and scintillation occurrence are intensified [11]. GPS observables and amplitude scintillation index (S_4) measurements were made at two different stations located in the city of São José dos Campos and 10.22 km apart. The stations are located near the southern crest of the EIA. Fig. 1(a) shows the position of the stations SJCE (blue dot) at S23.21° W45.86°, and SJCU (red dot) at S23.21°, W45.96°. The solid black/red lines correspond to the geomagnetic inclination/declination components around the stations. Although distance between stations was approximately 10.22 km, both stations reside in a very small area (green parallelogram) where the geomagnetic topology was the same. The analysis period was under quiet geomagnetic conditions, and the solar flux varied according to $141 \leq F10.7(\text{s.f.u.}) \leq 177$ in the maximum period of the solar cycle. It must be mentioned that in the eventual case of an EPB structure growing exactly along the region of the stations (early-stage structure) the gradient method used may not register the event; therefore, the method captures mostly the mature EPBs drifting over these regions.

The characterization presented in this article uses the ionospheric spatial gradient, which is a measure derived from comparing the measured TEC between two receivers, along with the complementary amplitude scintillation index, which is an indicator of the presence of EPBs. These parameters were obtained from Septentrio PolaRxS scintillation monitor receivers at stations SJCE and SJCU belonging to the CIGALA/CALIBRA network. GPS observables were recorded at every 15 s and amplitude scintillation index at rate of 50 Hz. For more details, please see [5]. Also, regional TEC maps were employed to support the analysis and to visualize the macroscopic behavior of the ionosphere. Data

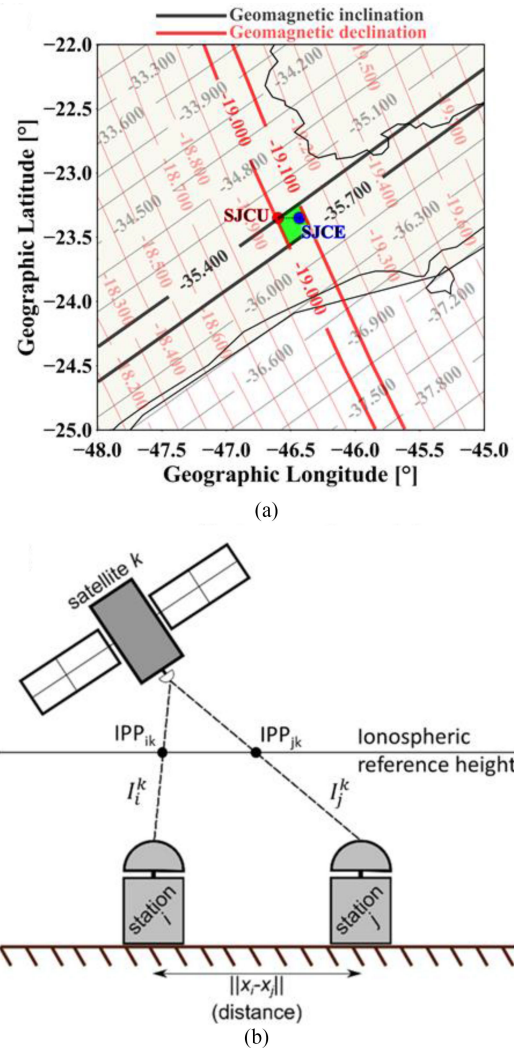


Fig. 1. Panel (a): Baseline direction between SJCU and SJCE stations. Panel (b): Diagram depicting the station-pair method used to calculate the ionospheric delay gradient. The difference of ionospheric delays calculated for each station based on measurements from the same satellite k at instant t , $|I_i^k(t) - I_j^k(t)|$, is divided by the distance between the stations, $\|x_i - x_j\|$.

from more than a 100 receivers from the Rede Brasileira de Monitoramento Contínuo dos Sistemas GNSS were used to produce these maps. See [18] and [6] for more details about these maps.

The ionospheric delay gradient was calculated according to (1) using the so-called station-pair method [12] depicted by Fig. 1(b) [31]. The ionospheric delay gradient at instant t , $\nabla I(t)$, is defined as the difference between the slant ionospheric delay (I) measured by two stations (i, j) from the same satellite k at the same time t divided by the norm of the distance between the stations, i.e.:

$$\nabla I(t) = \frac{|I_i^k - I_j^k|}{\|x_i - x_j\|} \quad (1)$$

where x_i and x_j are the positions of the stations i, j .

Slant ionospheric delay for each satellite, station, and time epoch was calculated from GPS observables stored in RINEX files, downloaded from the CIGALA/CALIBRA

server, with a sampling interval of 15 s. The computation was performed by the LTIAM (long-term ionospheric anomaly monitor) tool v2.2 [32]. In the calculation of ionospheric delay gradients, computed ionospheric delays based on carrier-phase measurements were used because carrier data has much lower noise than other measurements (e.g., pseudoranges), despite the integer ambiguities N_{L1} and N_{L2} present in the carrier for both $L1$ and $L2$ frequencies, respectively [31]. The carrier-derived slant ionospheric delay (I_ϕ) can be obtained from (2) [31], [29], where ϕ_{L1} and ϕ_{L2} are the carrier-phase observables in units of cycles, and λ_{L1} and λ_{L2} are the wavelengths in meters of the $L1$ and $L2$ frequencies, respectively:

$$I_\phi = \frac{\lambda_{L1}\phi_{L1} - \lambda_{L2}\phi_{L2}}{\gamma - 1} \quad (2)$$

$$\lambda_{L1}\phi_{L1} = r_i^k + c(b_i - B^k) + T_i^k - I_i^k + \lambda_{L1}N_{L1} + \varepsilon_{\phi_{L1}} \quad (3)$$

$$\begin{aligned} \lambda_{L2}\phi_{L2} &= r_i^k + c(b_i - B^k) + T_i^k - \gamma I_i^k \\ &\quad + c(IFB_i + \tau_{gd}^k) + \lambda_{L2}N_{L2} + \varepsilon_{\phi_{L2}} \end{aligned} \quad (4)$$

$$\gamma = \frac{f_{L1}^2}{f_{L2}^2} \quad (5)$$

where the receiver-satellite range (r_i^k), receiver and satellite clock biases (b_i and B^k), and tropospheric delay (T_i^k) are identical in (3) and (4) that show the components of the carrier observable for the $L1$ and $L2$ frequencies. Hence, these terms were automatically removed from the slant ionospheric delay calculation. Besides the carrier-phase integer ambiguities for both $L1$ and $L2$ frequencies, the receiver interfrequency bias (IFB $_i$) and satellite bias (τ_{gd}^k) must be estimated and removed to calculate ionospheric delays [31].

The algorithm for the calculation of the ionospheric delay used in the analysis presented in this article follows the flowchart shown in Fig. 2. Where from the file containing the ionospheric delay measurements processed by the LTIAM for the station i on the day of year d , we obtain the phase $I_\phi(t)$ and code $I_\rho(t)$ measurements for each visible satellite on that day. The algorithm processes the entire period of the satellite's sky pass above the elevation mask. Then the intervals in which there is an absence of phase measurements are identified and filled in with the code measurement values for the respective periods. The result of this step is the time series of the ionospheric delay $I(t)$ which is then processed by the function developed in the MATLAB® environment by [20] which implements the HANTS (harmonic analysis of time series) method [16] that is used to smooth the variability presented by code measures and obtain the series of the ionospheric delay $I_H(t)$. Finally, the ionospheric delay $I_o(t)$ is constructed from the phase $I_\phi(t)$ measurements obtained from the LTIAM file and the HANTS output data values that are used to fill the gaps where there is no data of phase.

HANTS allows the analysis of a time series as the superposition of sinusoidal functions expressed in terms of amplitude and harmonic frequencies, starting from the null frequency. The purpose of applying this method is to fill in the intervals with the absence of phase $I_\phi(t)$ measures and smooth the $I_\rho(t)$ code measures. Equation (6) presents the basic formula that describes the calculation of $I_H(t)$ as the

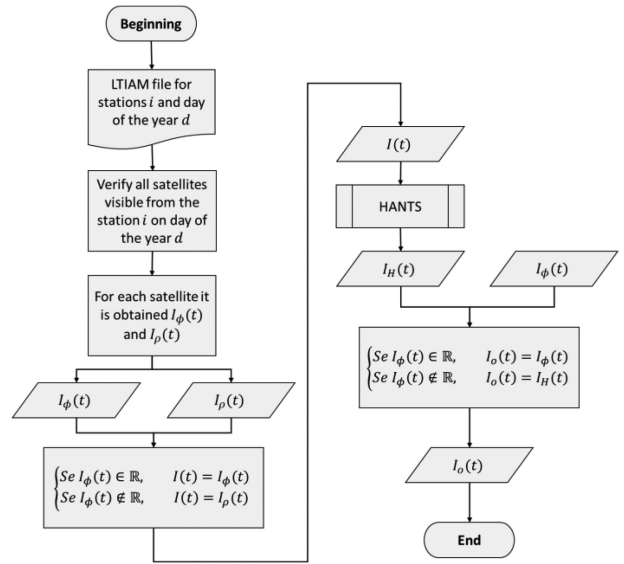


Fig. 2. Flowchart presents the time-series calculation of the slant ionospheric delay $I_o(t)$ used in the study presented in this article. $I_H(t)$ is after the application of the HANTS algorithm in the time series $I(t)$ built from the measurements of phase $I_\phi(t)$ and code $I_\rho(t)$ for the complete passage of each satellite seen by station i on the day of year d .

sum of sinusoidal functions, while the expression described in (7) presents the error $\varepsilon(t)$ that exists between the input data $I(t)$ of the HANTS algorithm and the output data [16]:

$$I_H(t) = a_0 + \sum_{i=1}^{nf} [a_i \cos(2\pi f_i t) + b_i \sin(2\pi f_i t)] \quad (6)$$

$$I(t) = I_H(t) + \varepsilon(t) \quad (7)$$

where t is the period in which satellite was visible above the elevation mask, nf is the number of harmonic frequencies considered in the Fourier analysis, a_i and b_i are the amplitude terms of the harmonic components of frequency f_i , and a_0 corresponds to the coefficient of null frequency which can be seen as the mean value of the series. The coefficients a_0 , a_i , and b_i are determined by the method of least squares in order to minimize the magnitude of the squared error $|\varepsilon|^2$ between the reconstructed series $I_H(t)$ and the original series $I(t)$ [16].

Carrier measurements are more susceptible to the effects of ionospheric disturbances and may encounter loss of lock or inconsistent readings, especially under severe scintillation events. These events are automatically removed by the LTIAM tool to prevent poor-quality data and false results. The issue of faulty results as a consequence of spurious ionospheric delay data is the main motivation for the article developed by [10]. The authors discuss the problem of poor-quality data and propose a methodology to minimize outliers. The method presented by [10] applies a series of metrics and takes advantage of dense networks to perform a well-distributed subnetwork selection obtaining satisfactory results. However, the networks available in Brazil are far from dense when compared to the ones used by [10]. Additionally, the number of stations available with the capability to measure the S_4 index is much lower. Also, what would be classified as poor-quality data, especially due

to the considerable occurrence of cycle-slips on the carrier-phase measurements, most of the times are caused by strong ionospheric interference, since it occurs systematically during the nighttime. This kind of data is often eliminated by the LTIAM resulting in significant data gaps exactly at periods that the ionospheric influence must be studied. Aiming at eliminating this issue and being able to count on continuous and reliable data, a solution was applied for this article. As mentioned earlier, when carrier measurements are not available, code measurements (pseudorange) are used, and the results are later processed by a filter based on HANTS, smoothing the noise of the code estimates. The code slant ionospheric delay (I_ρ) is calculated using (8) [31], [29]:

$$I_\rho = \frac{\rho_{L2} - \rho_{L1}}{\gamma - 1} \quad (8)$$

$$\rho_{L1} = r_i^k + c(b_i - B^k) + T_i^k + I_i^k + \varepsilon_{\rho_{L1}} \quad (9)$$

$$\rho_{L2} = r_i^k + c(b_i - B^k) + T_i^k + \gamma I_i^k + c(IFB_i + \tau_{gd}^k) + \varepsilon_{\rho_{L2}}. \quad (10)$$

Measurements made by GNSS receivers in low-latitude regions require special attention because strong scintillation events may result in corruption of the ionospheric gradient data. The LTIAM tool provides a function to detect cycle slips and to remove short arcs and outliers. Cycle slip detection is done using three different approaches: 1) detection of a large jump between two adjacent points, 2) loss of lock indicator recorded in the RINEX file, and 3) absence of $L1$ and $L2$ carrier measurements [32]. After detecting the cycle slips, LTIAM removes short arcs because, according to [32], leveling short arc would lead to large errors, making the delay estimates useless. The outliers are identified for each continuous arc using a polynomial fit and adjacent point difference methods, and then, they are removed from the output data [32]. Furthermore, all the ionospheric delay estimations were carefully analyzed based on the thorough examinations carried out in the validation of [26] and supported by regional maps.

As mentioned earlier, during EPB events, large depletions may be found along the signal path. These events are typically observed as amplitude scintillation evaluated through the S_4 index. EPB event may also be found in the form of a sudden change in TEC, i.e., a large TEC gradient. The S_4 index indicates the strength of the variation in the amplitude of the received signal, typically measured every minute, and is given by (11) [7]:

$$S_4 = \frac{\sqrt{\langle I^2 \rangle - \langle I \rangle^2}}{\langle I \rangle} \quad (11)$$

with $\langle \dots \rangle$ representing the average value for 60 s, where $I = |R^2|$ is the receiver signal intensity over those 60 s, and R is the amplitude of the signal with sample rate of 50 Hz.

In this case, there are four available estimates of ionospheric delay gradient per minute. The sample with the maximum value over each minute was used to evaluate the correlation between the S_4 index and the ionospheric delay slope. It is important to mention that measurements of ionospheric delay and gradients have a resolution of 15 s, while the S_4 index has a resolution of 60 s. Hence, there will be four gradient measures for each value of S_4 . In this article, it was assumed that an $S_4 \geq 0.3$ implies the occurrence of

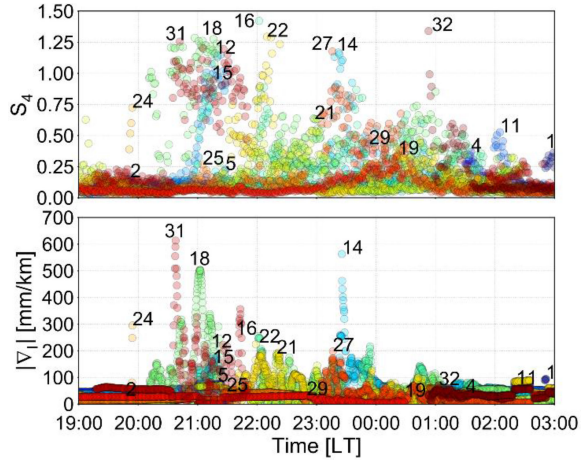


Fig. 3. Top panel: S_4 index obtained from the available GPS satellites for the station SJCU during the night between November 17 and 18, 2014. Bottom panel: The respective ionospheric gradients, $|\nabla I|$, for the same night between stations SJCU and SJCE.

tangible scintillation indicating the presence of EPBs, while $S_4 \geq 0.7$ corresponds to a severe event [2], [3], [21].

Fig. 3 shows one example for the night between November 17 and 18, 2014. The top panel shows the S_4 index recorded between 19:00 and 03:00 LT for the SJCU station considering all available GPS satellites. It is possible to observe large values of amplitude scintillation, indicating the existence of EPB events. During these events, strong scintillation ($S_4 \geq 0.7$) was mostly concentrated between 20:00 and 00:00 LT but was not restricted to this period. The bottom panel of Fig. 3 shows the respective absolute value of ionospheric gradients between SJCU and SJCE stations, $|\nabla I|$. We can observe the occurrence of $|\nabla I|$ significantly exceeding 400 mm/km for some satellites during early nighttime.

This introductory result suggests that under the same EPB event, with similar scintillation occurrence, distinct satellites experienced different spatial gradients. These dissimilarities seem to be related to the orientation of the propagation path of a given GPS signal across the plasma bubble region. In the next section, the relationship between cases with large gradients and EPB structures represented by large values of the S_4 index will be discussed.

III. EPBS AND ASSOCIATED IONOSPHERIC GRADIENTS

Previous articles, such as [24], [21], show a direct relationship between EPB events and ionospheric spatial gradients. In this section, this interconnection is further explored by examining the 16 nights of available data from November 2014. Estimated ionospheric spatial gradients in this data were grouped into four distinct bins, namely, $0 < |\nabla I| \leq 200$, $200 < |\nabla I| \leq 400$, $400 < |\nabla I| \leq 600$, and $600 > |\nabla I|$, in units of mm/km.

Fig. 4 shows the distribution of S_4 scintillation index values for these four distinct ranges of $|\nabla I|$. The histogram in the top-left panel of Fig. 4 shows that, during gradients within the range $0 < |\nabla I| \leq 200$ mm/km, the observed scintillation is very weak or absent, being concentrated in the range of $S_4 \leq 0.3$. In the histogram in the top-right panel, for gradients in the range $200 < |\nabla I| \leq 400$ mm/km, the distribution of S_4

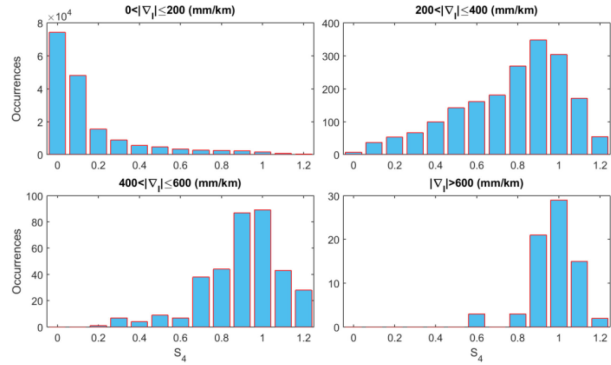


Fig. 4. Histogram showing the number of scintillation occurrences for distinct ranges of ionospheric gradients $|\nabla I|$.

values changes substantially, with a gradual increase in the number of cases with larger values of S_4 that peak around $S_4 = 0.9$. This behavior suggests that increasing values of S_4 ($0.3 \leq S_4 \leq 0.9$) are related to more often occurrence of $200 < |\nabla I| \leq 400$ mm/km.

The bottom-left panel of Fig. 4 shows the occurrences of S_4 for the range $400 < |\nabla I| \leq 600$ mm/km. This range exceeds the level of 400 mm/km, which is approximately the upper bound of the GBAS ionospheric threat model for CONUS. The relationship between large gradients and strong amplitude scintillation is clear, as the scintillation index values are concentrated at $S_4 \geq 0.7$. There is some attenuation for very large values of S_4 , which is expected due to the limited number of events with extremely large S_4 . Finally, the bottom right panel shows the extreme spatial gradient events for the range $|\nabla I| > 600$ mm/km. During these events, only very large values of S_4 were registered.

The distributions of S_4 according to different ranges of ionospheric delay gradients presented in Fig. 4 show that cases of $|\nabla I| > 400$ mm/km are typically related to strong scintillation events, typically with $S_4 \geq 0.7$. These results also indicate that signals from satellites whose lines of sight to receivers are not affected by EPBs do not present large ∇I values. Fig. 5 shows an example of four regional maps of vertical TEC during the night between November 16 and 17, 2014. Satellite PRNs 2, 4, 5, 6, 10, and 19 are examples of ray paths with no EPB influences. At the one hand, these satellites were in the southeastern sky, beyond the EIA, and out the EPB structures extension. On the other hand, the other satellites with ionospheric pierce points (IPPs) around the EIA peak region, also coincide with the region affected by EPB depletions, therefore experiencing large gradients due to the depletion caused by the EPBs in the region of large density (due to the EIA). In Fig. 5, the IPPs (black circles) and TEC (cold to hot colors) at distinct instants reveal that, between 22:00 and 24:00 LT, signatures of EPBs (depleted streaks) are already present across the EIA region along the ray path of several satellite links. These regions are the likely sources of strong spatial gradients. For more details on EPB signatures in TEC maps, please see [6], [18].

The above results suggest that extreme ionospheric spatial gradients are related to strong amplitude scintillation. Due to the half-sidereal-day orbit periods of the satellites in the GPS constellation, the satellite IPPs will be approximately at the same position, slightly shifted, at the same time on the following day. In other words, signals from the same satellites pass through the EIA region during the analysis

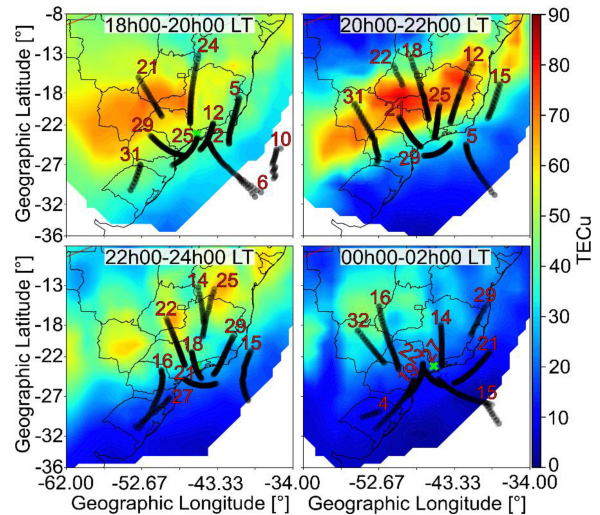


Fig. 5. Ionospheric TEC maps between 18:00 and 02:00 LT during the night between November 16 and 17, 2014. The maps show several IPPs (black circles) along the EIA region (hotter colors). The initial smoother distribution of the TEC is disrupted by elongated depleted streaks known as EPBs (colder colors). The presence of these EPB structures causes scintillation and creates large density gradients along the EIA region. The SJCU station is indicated by the green cross for visual reference.

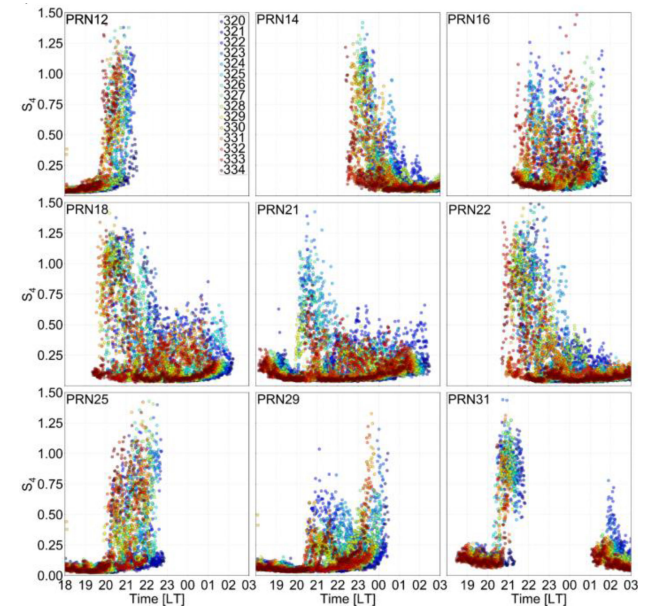


Fig. 6. SJCU measurements of S_4 from all visible GPS satellites over the EIA region for the nights between 15 and 30 November 2014 according to local time. The legend in the upper-left plot indicates which color corresponds to each day of the year.

period. The panels in Fig. 6 show the S_4 index measured at station SJCU for all satellites whose IPPs cross the EIA region in the analysis period according to what is shown in Fig. 5. The data gaps in Fig. 6 correspond to the period when the satellite elevation was below the elevation mask of 12° . These panels indicate a general trend of scintillation onset time, typically around 20:00 LT, with a considerable decline of scintillation (and consequently EPB activity) as later times at night are considered, especially for PRNs 14, 18, 21, and 22. These onset times are in agreement with the literature [3], [11], and the observed decline in scintillation

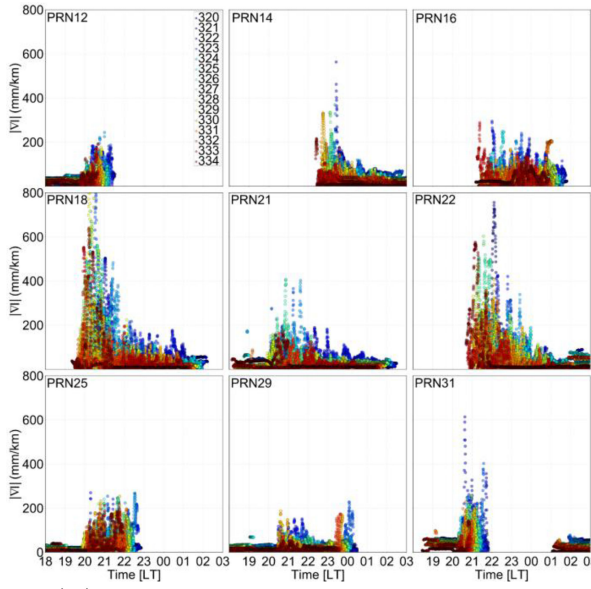


Fig. 7. $|\nabla I|$ calculated by the station-pair method with data from the same GPS satellites and cases as Fig. 6 as observed by the SJCU and SJCE stations. The legend indicates which color corresponds to each day of the year.

is expected since the development of plasma instabilities and EPBs take place in the early nighttime scenario, when the instability is mainly driven by the $\vec{E} \times \vec{B}$ drift. Later, the collision frequency dominates, and the instability reaches the topside [22]. In any case, the relation of these events with the magnitude of the ionospheric gradients deserves special attention.

The panels in Fig. 7 show the respective ionospheric gradients calculated from the measurements at SJCU and SJCE stations for the same satellites and periods using the station-pair method. Fig. 7 shows that, in general, large ionospheric gradients occurred concurrently with the scintillation/EPB events detected by the S_4 index in Fig. 6. Although all PRNs presented large gradients almost simultaneously with high S_4 measurements, the critical events, i.e., those with $|\nabla I| > 400$ mm/km, were observed mostly on PRNs 18 and 22.

The top panel of Fig. 8 shows the total number of occurrences at station SJCU of $S_4 \geq 0.3$ for each PRN, indicating the number of minutes (i.e., S_4 measurement epochs) that the signal from a given satellite is thought to have been affected by EPBs over during the analyzed period of 16 nights. The middle panel is similar but showing only the occurrences of $S_4 \geq 0.7$, referred to as strong scintillation events. The bottom panel shows the number of occurrences (measured every 15 s) of critical ionospheric gradients, $|\nabla I| > 400$ mm/km, for the SJCU–SJCE station pair over the same data period and reveals that these events are mostly concentrated on satellite PRNs 18 and 22.

The top and middle panels reveal that all satellites with IPPs in the EIA region suffered scintillation, sometimes reaching $S_4 \geq 0.7$, which agrees with the maps in Fig. 5. Despite all these satellites experiencing large scintillation, occurrences of $|\nabla I| > 400$ mm/km are concentrated on PRNs 18 and 22, with 287 and 142 cases, respectively. Note that PRN 31 experienced almost as many cases of $S_4 \geq 0.7$ (572) as did each of PRNs 18 (760) and 22 (676) but

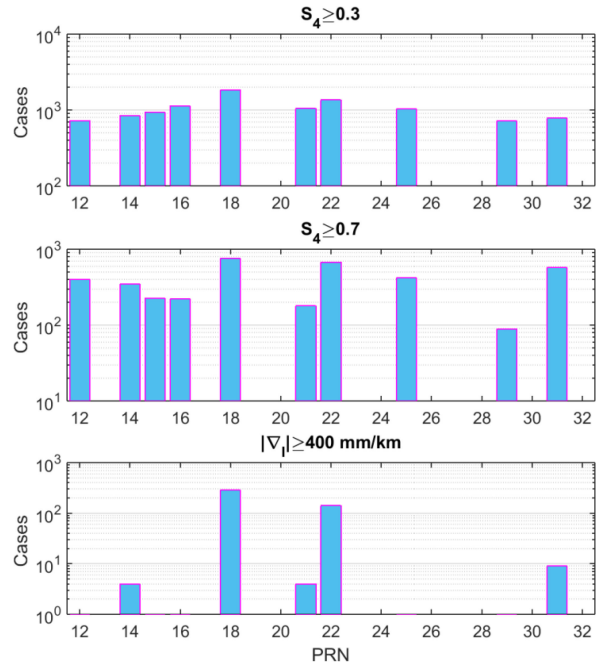


Fig. 8. Histogram of $S_4 \geq 0.3$ (top) and $S_4 \geq 0.7$ (middle) signal occurrences per satellite (PRN) at station SJCU. Bottom panel: Histogram of the critical ionospheric gradients, $|\nabla I| > 400$ mm/km, according to the station-pair method for SJCU and SJCE stations.

observed only nine cases with $|\nabla I| > 400$ mm/km. A discussion on the processes behind this behavior is presented in the following section.

IV. ALIGNMENT EFFECTS

The work of [1] and [33] used azimuth and elevation data during scintillation events measured by GPS stations in India and showed an increase in strong scintillation cases when GPS signals was aligned with EPB structures. Using data from São José dos Campos, [3] and [2] also reported concentrations of extreme scintillation events when the signal propagation path is aligned with EPB structures. Moreover, [2] provided a statistical analysis of the increase in scintillation under EPB alignment as well as consequences on GPS receivers such as signal fading, loss-of-lock, and errors in precise point positioning. EPB alignment occurs when the azimuth and elevation angles of the satellite-receiver line of sight are approximately parallel to the magnetic meridian and inclination, respectively. This is because EPBs propagate along the geomagnetic field lines; hence, the spatial distribution of these depleted regions depends on the field lines morphology. The analysis presented in this section focuses on ionospheric spatial decorrelation and its relationship with enhanced scintillation events when the GPS-receiver line of sight is aligned with EPBs, in orther words, aligned with geomagnetic field.

In order to assess alignment geometrically, two angles were calculated according to [2]. The first corresponds to the difference between the elevation angle of the signal path and the geomagnetic field inclination angle at the IPP. The second corresponds to the difference between the azimuth angle of the signal path and the geomagnetic field declination angle at the IPP. In this article, the received signal was considered to be aligned when both of these angle

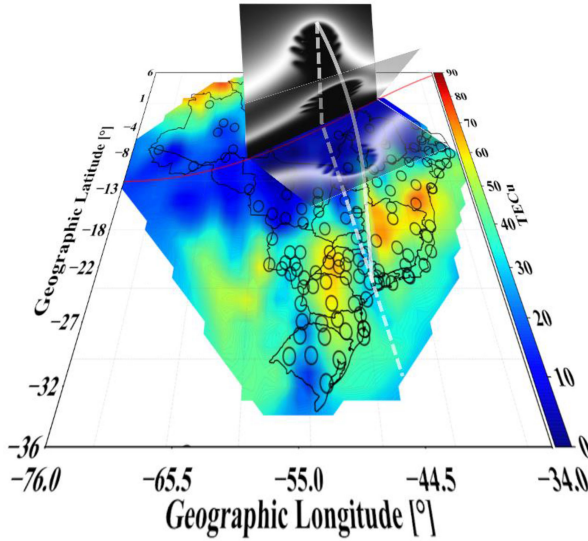


Fig. 9. Pictorial representation of the EPB development (black structure) and propagation to off-equator latitudes. The solid white arc represents a geomagnetic field line connecting the equatorial region to the EIA region. The dashed white line indicates the approximate projection of the EPB propagation. The color map describes the TEC concentration; darker elongated streaks correspond to EPB depleted regions.

differences are $\leq 15^\circ$. The geomagnetic field inclination and declination angles were estimated based on IGRF-12 [8].

Fig. 9 illustrates EPB development and propagation. The black structure rising over the equatorial region (solid red line) represents an EPB structure crossing the region with larger plasma density (represented by the white color). The EPB develops along the geomagnetic field lines (represented by the white arc), eventually reaching the EIA region (hot colors in the TEC map). The black circles correspond to ground stations from which TEC data are obtained. The white dashed line represents approximately the angle of geomagnetic declination along the depicted EPB propagation path. The alignment between the satellite signal path azimuth and the geomagnetic declination indicates that the signal crosses a slab of the EPB in the plane described by the longitudes and latitudes at the specific altitude of the IPP. The geomagnetic inclination depends on the angle between the geomagnetic field line at a given point and the horizontal surface plane below that point. Hence, the alignment between satellite elevation and geomagnetic inclination indicates that the signal path intersects a portion of the EPB structure in the vertical/meridional direction around the altitude/latitude of the IPP.

An analysis was performed to verify which satellite paths were aligned during the period under study. According to the results, PRNs 18, 22, 24, and 27 matched the requirements to be considered aligned (i.e., angle differences were $\leq 15^\circ$) over the stations at São José dos Campos for an IPP altitude of 350 km. Fig. 10 shows the time window in which this condition was met on each day within the dataset. By comparing the time intervals in Fig. 10 with the events presented in Figs. 6 and 7, it is possible to conclude that, although PRNs 24 and 27 were aligned, no EPB was detected during the passes of these satellites. Therefore, for the analyzed period, the satellites that met the conditions as mentioned earlier of alignment concurrent with EPB events

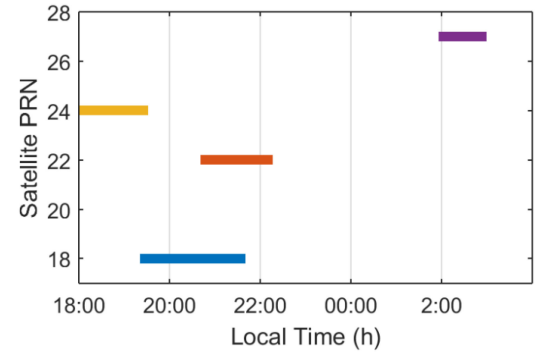


Fig. 10. Time windows during which PRNs met the alignment condition within the period of analysis. Although PRNs 24 and 27 were aligned, no EPB events were intersected by their signals.

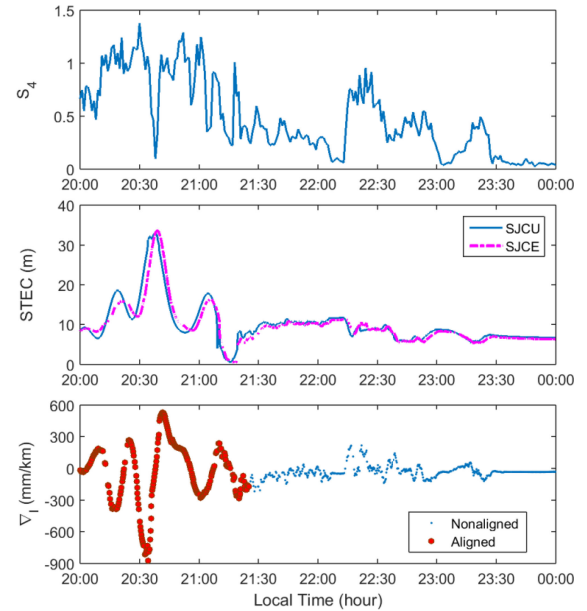


Fig. 11. Example of alignment effects on PRN 18 on the night of November 19, 2014. Top panel: S_4 index experienced at SJCU station, revealing the occurrence of scintillation since early nighttime. Middle panel: slant ionospheric delay/STEC obtained at SJCU and SJCE stations. Bottom panel: Ionospheric gradient ∇I during aligned and nonaligned conditions.

were PRNs 18 and 22. These satellites have shown to be the most affected by large gradients, as presented in Fig. 8.

Considering these results, an assessment of the environmental influence on the formation of ionospheric gradients was performed. The measurements from PRN 18 on the night of November 19, 2014 were used as an evaluation example, and the results are presented in Fig. 11. The top panel shows the degree of amplitude scintillation along the early nighttime hours for the SJCU station. The S_4 index indicates that the signal was affected by ionospheric irregularities since the beginning of the time interval shown by Fig. 11. Notwithstanding, suddenly, between 20:35 and 20:40 LT, the values of S_4 decreased steeply, then increased again and remained around $S_4 = 0.8$ up to 21:04 LT. This sudden change probably was caused due to the transition from an EPB to a non-EPB region. The middle panel shows the slant TEC (STEC) or slant ionospheric delay estimates for stations SJCU (blue) and SJCE (magenta) in units of

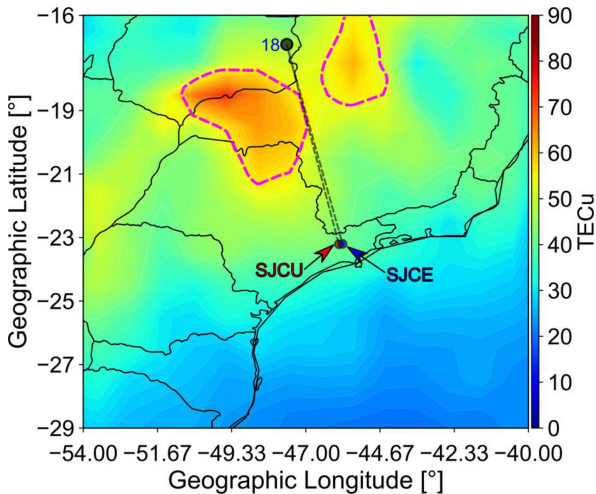


Fig. 12. Regional map (vertical TEC) showing the alignment condition for the signal received from satellite PRN 18 at 20:30 LT during the night of November 19, 2014.

meters. Correlating the STEC data with the S_4 observed in the top panel reveals that the sudden drop of S_4 occurred at the moment when the STEC values experienced an increase of ~ 30 m. The bottom panel shows the estimated ∇I from the STEC data from SJCU and SJCE presented in the middle panel. In the interval between 20:35 and 20:40 LT, the magnitude of the ∇I values increased considerably and reached an extreme value of -874.7 mm/km. Immediately after 20:40 LT, when S_4 increased again and STEC decreased approximately 10 m, another severe gradient occurs, this time reaching 527.8 mm/km.

Fig. 12 shows a regional map with vertical TEC values based on the method of [18] at 20:30 LT on November 19, 2014, and complements the results exhibited in Fig. 11. The TEC map indicates that the IPP of PRN 18 is intersecting an EPB. However, slightly southwest of the IPP, there is a concentration of high TEC in the EIA region (highlighted by the magenta dashed curve). This region is the possible cause of the sudden increase in STEC and the subsequent generation of the critical gradient between the stations considered.

Continuing the analysis, a comparison between the critical gradients under aligned and nonaligned environments is presented for the entire analysis period. The top panel of Fig. 13 shows the total number of aligned (dark blue) and nonaligned (cyan) epochs with $|\nabla I| > 400$ mm/km per night over all received satellite signals. The night with most epochs was November 30, 2014 (day-of-year, DOY, 334), when the number of aligned epochs was 68 and the number of nonaligned epochs was 10, giving a total of 78 epochs. The majority of cases were also aligned during the nights of DOY 321 and 326. During the period of analysis covering 16 nights, there were no critical gradient events in only two of them, namely on the nights of DOY 331 and 332. There were no aligned cases on two nights, DOY 322 and 324, but seven epochs with critical gradients occurred under nonaligned conditions on each of these nights. These results show the relevance of considering the degree of signal-to-EPB alignment in the analysis of large spatial ionospheric gradients for safety-critical applications like GBAS.

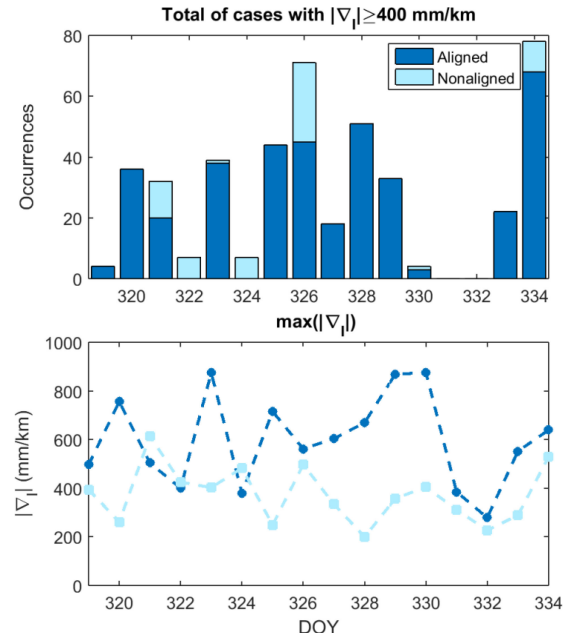


Fig. 13. Top panel: comparison of occurrences of critical gradient events under aligned (dark blue) and nonaligned (cyan) conditions. Bottom panel: maximum absolute value of gradient per night under aligned (dark blue) and nonaligned (cyan) conditions.

The bottom panel of Fig. 13 presents the maximum value of $|\nabla I|$ per night. The results indicate that, beyond the significant number of critical gradient events caused by alignment condition, their maximum absolute values (dark blue) were typically larger than in nonaligned cases (cyan). On three nights (DOY 323, 329, and 330), $|\nabla I|$ under alignment exceeded 850 mm/km, denoting extreme gradient events, whose magnitude is twice the maximum value defined in the CONUS threat model [31].

Fig. 14 shows the statistics of cases of ionospheric gradient magnitudes for the two stations considered (SJCU and SJCE). The top panel presents the complementary cumulative distribution function (CCDF) of $|\nabla I|$. The blue solid line is the CCDF considering the entire nighttime period from 18:00 to 03:00 LT. However, as observed in Figs. 6 and 7, most critical gradient events occurred between 20:00 and 00:00 LT. Hence, the CCDF for this time interval is also presented in the form of a red dashed line. As mentioned earlier, EPBs are more often observed during the early nighttime period between 20:00 and 00:00 LT, and critical ionospheric gradient events are directly related to the existence of these depleted structures as well as to signal alignment conditions. The CCDF for this early nighttime period indicates a probability of $|\nabla I| > 400$ mm/km of approximately 0.5%, whereas the same probability for the entire nighttime period is around 0.21%.

The bottom panel shows the CCDF considering the presence or absence of EPBs and satellite signal alignment with EPB propagation. The orange dotted curve shows the probability of $|\nabla I|$ in the absence of bubbles, which is assumed to be the case when $S_4 < 0.3$. In this situation, no critical gradients are expected, and the probability of $|\nabla I| > 200$ mm/km is less than 0.1%. The dashed cyan curve represents the probabilities in cases with EPBs assumed to be present (when $S_4 \geq 0.3$), but without the alignment

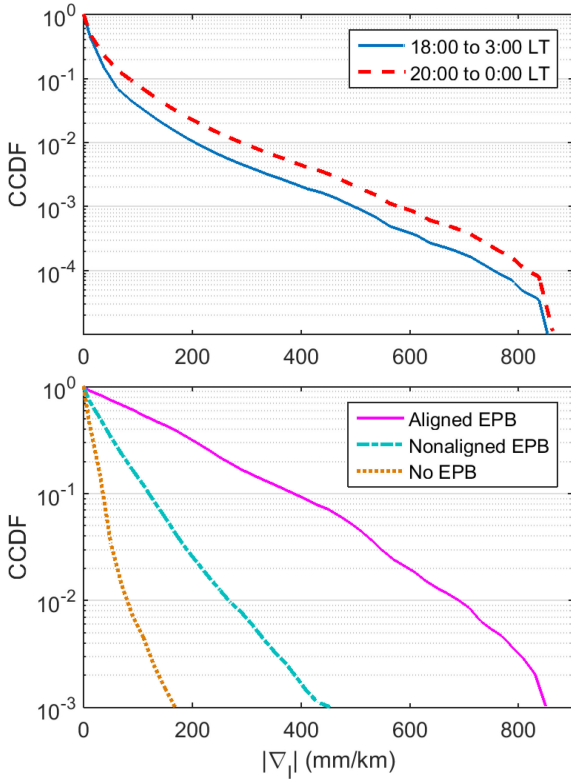


Fig. 14. Probabilities of ionospheric gradient magnitudes observed at SJCU and SJCE stations over the period from November 15 to 30, 2014. Top panel: CCDF of $|\nabla I|$ from 18:00 to 3:00 LT (solid blue curve) and from 20:00 to 0:00 LT (the red dashed line). Bottom panel: CCDF under 3 scenarios: 1) no EPBs (orange curve); 2) EPBs but nonaligned signals (cyan dashed line); and 3) EPBs and aligned signals (solid magenta line).

condition. The observed probability of events with $|\nabla I| > 400$ mm/km is approximately 0.2%, while for events with $|\nabla I| > 200$ mm/km it reaches about 2.5%. This result suggests that signals intersecting EPBs under nonaligned conditions are unlikely to exhibit critical spatial gradients, although exceptions may occur. Finally, the magenta curve shows the results with EPBs assumed to be present during alignment conditions. The difference in statistics for this particular configuration is significant, and the probability of $|\nabla I| > 400$ mm/km is around 10%. This probability expresses a troublesome scenario for applications such as augmentation systems operating under similar conditions. For extreme events with $|\nabla I| > 600$ and $|\nabla I| > 800$ mm/km, the probabilities are approximately 2 and 0.3%, respectively. Such high CCDF values for the aligned EPB configuration indicate that knowledge of the degree of alignment (if an EPB exists) is important information for assessing the ionospheric gradient threat to safety-critical applications of GNSS.

V. CONCLUSION

In this article, the amplitude scintillation index and the ionospheric spatial gradients observed by two stations located in São José dos Campos during the nights (18:00 to 03:00 LT) from November 15 to 30, 2014 were analyzed. The period of analysis was under quite geomagnetic and high solar flux conditions. The results showed strong scintillation events after 20:00 LT on some nights for almost

all satellites in view. The occurrence of large ionospheric gradients increased according to the amplitude scintillation index, suggesting a direct relation between these two metrics. Critical gradients, those larger than 400 mm/km, occurred only for the satellite PRNs 14, 18, 21, 22, and 31, mainly on PRNs 18 and 22, on 287 and 142 measurement epochs, respectively.

In the early nighttime hours (20:00 and 00:00 LT), PRNs 18 and 22 were found to be in alignment with the depleted EPB structures causing scintillation. On most nights, the aligned cases correlate with larger magnitudes of ionospheric spatial decorrelation and increased occurrences of critical gradients exceeding 400 mm/km. Statistical analysis showed that a GNSS user in the vicinity of São José dos Campos had a probability of experiencing critical ionospheric gradients reaching $\sim 10\%$ in the early nighttime period for satellite signals aligned with EPBs. For nonaligned signals, this probability is only about 0.2%. The results presented here suggest a strong relationship between extreme ionospheric spatial decorrelation and GNSS signals alignment with EPBs. Similar evaluations presented in earlier article such as [1], [2], and [33] were primarily based on scintillation data. The relation between EPBs, scintillation, critical ionospheric gradients, and the GNSS signal alignment were further addressed in this article. The conclusions of this article are believed to reflect the overall behavior of the ionosphere over low latitudes and are not specific to or limited to the study site.

The characterization of observed gradients in terms of alignment with the geomagnetic field allows narrowing down and better understanding threatening conditions for GBAS and other safety-critical applications of GNSS. In particular, this characterization is potentially beneficial in developing improved ionospheric threat models and mitigation strategies for GBAS in low latitudes. Notwithstanding, for safety-critical applications the nonaligned large gradients cases are also of great importance. Although this article reveals that these events are less frequent, future investigations are required to understand the mechanism behind these unexpected occurrences.

ACKNOWLEDGMENT

The authors are grateful to Instituto Brasileiro de Geografia e Estatística for providing GPS data from Rede Brasileira de Monitoramento Contínuo for the construction of TEC maps of Figs. 5, 9, and 12. They are also grateful to M.Sc. L. A. Salles, Prof. E Costa, Dr. M. A. Abdu, and Prof. J. F. Galera Monico for their comments and suggestions. They would also like to thank the reviewers for the insightful and constructive comments.

REFERENCES

- [1] A. DasGupta, S. Ray, A. Paul, P. Banerjee, and A. Bose
Errors in position-fixing by GPS in an environment of strong equatorial scintillations in the Indian zone
Radio Sci., vol. 39, no. 1, pp. 1–8, Feb. 2004.
- [2] A. O. Moraes *et al.*
GPS availability and positioning issues when the signal paths are aligned with ionospheric plasma bubbles
GPS Solutions, vol. 22, no. 4, Jul. 2018, Art. no. 95.

- [3] A. O. Moraes *et al.* The variability of low-latitude ionospheric amplitude and phase scintillation detected by a triple-frequency GPS receiver *Radio Sci.*, vol. 52, no. 4, pp. 439–460, Apr. 2017.
- [4] Annex 10 to the convention on international civil aviation - Aeronautical Telecommunications, volume i – radio navigation aids Amendment, vol. 92, ICAO Annex 10, 2020.
- [5] B. C. Vani, M. H. Shimabukuro, and J. F. G. Monico Visual exploration and analysis of ionospheric scintillation monitoring data: The ISMR query tool *Comput. Geosci.*, vol. 104, pp. 125–134, Jul. 2017.
- [6] C. B. Oliveira *et al.* Analysis of plasma bubble signatures in total electron content maps of the low-latitude ionosphere: A simplified methodology *Surv. Geophys.*, vol. 41, no. 4, pp. 897–931, Mar. 2020.
- [7] C. Y. Kung and L. Chao-Han Radio wave scintillations in the ionosphere *Proc. IEEE*, vol. 70, no. 4, pp. 324–360, Apr. 1982.
- [8] E. Thébault *et al.* International geomagnetic reference field: The 12th generation *Earth Planet Space*, vol. 67, no. 1, May 2015, Art. no. 79.
- [9] J. Cho, Y. Yun, and M. Heo GBAS ionospheric anomaly monitoring strategy using Kullback–Leibler divergence metric *IEEE Trans. Aerosp. Electron. Syst.*, vol. 51, no. 1, pp. 565–574, Jan. 2015.
- [10] J. Lee and M. Kim Optimized GNSS station selection to support long-term monitoring of ionospheric anomalies for aircraft landing systems *IEEE Trans. Aerosp. Electron. Syst.*, vol. 53, no. 1, pp. 236–246, Feb. 2017.
- [11] J. Lee, J. Seo, Y. S. Park, S. Pullen, and P. Enge Ionospheric threat mitigation by geometry screening in ground-based augmentation systems *J. Aircr.*, vol. 48, no. 4, pp. 1422–1433, Aug. 2011.
- [12] J. Lee, S. Pullen, S. Datta-Barua, and P. Enge Assessment of nominal ionosphere spatial decorrelation for GPS-based aircraft landing systems *J. Aircr.*, vol. 44, no. 5, pp. 1662–1669, Oct. 2007.
- [13] J. Patel, S. Khanafseh, and B. Pervan Detecting hazardous spatial gradients at satellite acquisition in GBAS *IEEE Trans. Aerosp. Electron. Syst.*, vol. 56, no. 4, pp. 3214–3230, Aug. 2020.
- [14] J. Seo, T. Walter, and P. Enge Availability impact on GPS aviation due to strong ionospheric scintillation *IEEE Trans. Aerosp. Electron. Syst.*, vol. 47, no. 3, pp. 1963–1973, Jul. 2011.
- [15] J. Sousasantos, A. O. Moraes, J. H. Sobral, M. T. Muella, E. R. de Paula, and R. S. Paolini Climatology of the scintillation onset over Southern Brazil *Annales Geophysicae*, vol. 36, no. 2, pp. 565–576, Apr. 2018.
- [16] J. Zhou, L. Jia, and M. Menenti Reconstruction of global MODIS NDVI time series: Performance of harmonic analysis of time series (HANTS) *Remote Sens. Environ.*, vol. 163, pp. 217–228, Jun. 2015.
- [17] L. A. Salles, B. C. Vani, A. Moraes, E. Costa, and E. R. de Paula Investigating ionospheric scintillation effects on multifrequency GPS signals *Surv. Geophys.*, vol. 42, pp. 999–1025, Apr. 2021.
- [18] L. Marini-Pereira, L. F. D. Lourenço, J. Sousasantos, A. O. Moraes, and S. Pullen Regional ionospheric delay mapping for low-latitude environments *Radio Sci.*, vol. 55, no. 12, pp. 1–16, Dec. 2020.
- [19] L. Marini-Pereira, S. P. Pullen, and A. de Oliveira Moraes Reexamining low-latitude ionospheric error bounds: An SBAS approach for Brazil *IEEE Trans. Aerosp. Electron. Syst.*, vol. 57, no. 1, pp. 674–689, Feb. 2021.
- [20] M. Abouali MATLAB implementation of harmonic ANalysis of time series (HANTS) MATLAB Central File Exchange Version 1.0.0.0, 2012. Accessed: Sep. 22, 2020. [Online]. Available: <https://www.mathworks.com/matlabcentral/fileexchange/38841-matlab-implementation-of-harmonic-analysis-of-time-series-hants>
- [21] M. Harris, T. Murphy, and S. Saito Further validation of GAST d ionospheric anomaly mitigations In *Proc. Int. Tech. Meeting Inst. Navigation*, 2011, pp. 942–949.
- [22] M. C. Kelley, K. D. Baker, and J. C. Ulwick Late time barium cloud striations and their possible relationship to equatorial spread F *J. Geophys. Res.: Space Phys.*, vol. 84, no. A5, pp. 1898–1904, May 1979.
- [23] M. Yoon, D. Kim, and J. Lee Extreme ionospheric spatial decorrelation observed during the March 1, 2014, equatorial plasma bubble event *GPS Solutions*, vol. 24, no. 2, Feb. 2020, Art. no. 47.
- [24] M. Yoon, D. Kim, and J. Lee Validation of ionospheric spatial decorrelation observed during equatorial plasma bubble events *IEEE Trans. Geosci. Remote Sens.*, vol. 55, no. 1, pp. 261–271, Jan. 2017.
- [25] M. Yoon, D. Kim, S. Pullen, and J. Lee Assessment and mitigation of equatorial plasma bubble impacts on category I GBAS operations in the Brazilian region *Navigation*, vol. 66, no. 3, pp. 643–659, Aug. 2019.
- [26] M. Yoon *et al.* Equatorial plasma bubble threat parameterization to support GBAS operations in the brazilian region *Navigation*, vol. 64, no. 3, pp. 309–321, Sep. 2017.
- [27] *Minimum Operational Performance Standards for GPS/Local Area Augmentation System Airborne Equipment*. Washington, DC, USA: RTCA, Jul. 13, 2017.
- [28] N. Linty, A. Farasin, A. Favenza, and F. Dovis Detection of GNSS ionospheric scintillations based on machine learning decision tree *IEEE Trans. Aerosp. Electron. Syst.*, vol. 55, no. 1, pp. 303–317, Feb. 2019.
- [29] P. Misra and P. Enge *Global Positioning System: Signals, Measurement, and Performance*, 2nd ed. Lincoln, MA, USA: Ganga-Jamuna Press, 2006.
- [30] S. Datta-Barua Ionospheric threats to space-based augmentation system development In *Proc. 17th Int. Tech. Meeting Satell. Division Inst. Navigation*, 2004, pp. 1308–1317.
- [31] S. Datta-Barua *et al.* Ionospheric threat parameterization for local area global-positioning-system-based aircraft landing system *J. Aircr.*, vol. 47, no. 4, pp. 1141–1151, Aug. 2010.
- [32] S. Jung and J. Lee Long-term ionospheric anomaly monitoring for ground based augmentation systems *Radio Sci.*, vol. 47, no. 4, Jul. 2012, Art. no. RS4006.
- [33] S. Ray, U. Bhowmik, and A. Das Scintillation effects related to propagation geometry as applicable to Indian SBAS In *Proc. 31st URSI Gen. Assem. Sci. Symp.*, 2014, pp. 1–4.
- [34] S. Saito *et al.* Ionospheric delay gradient model for GBAS in the Asia-Pacific region *GPS Solutions*, vol. 21, no. 4, pp. 1937–1947, Sep. 2017.

- [35] S. Saito, T. Yoshihara, and N. Fujii
Study of effects of the plasma bubble on GBAS by a three-dimensional ionospheric delay model
In Proc. 22nd Int. Tech. Meeting Satell. Division Inst. Navigation, 2009, pp. 1141–1148.
- [36] T. E. Humphreys, M. L. Psiaki, and P. M. Kintner
Modeling the effects of ionospheric scintillation on GPS carrier phase tracking
IEEE Trans. Aerosp. Electron. Syst., vol. 46, no. 4, pp. 1624–1637, Oct. 2010.
- [37] Y. Jiao, J. J. Hall, and Y. T. Morton
Automatic equatorial GPS amplitude scintillation detection using a machine learning algorithm
IEEE Trans. Aerosp. Electron. Syst., vol. 53, no. 1, pp. 405–418, Feb. 2017.

Bruno Jacobini Affonso received the B.S. degree in electrical engineering from Universidade Estadual Paulista, Bauru, Brazil, in 2012, and the M.Eng. degree in aerospace engineering from the Instituto Tecnológico de Aeronáutica, São José dos Campos, Brazil, in 2016, where he is currently working toward the Ph.D. degree in electronics and computer engineering program.

Additionally, he worked for almost 8 years as a Product Development Engineer with EMBRAER where he was the Lead System Engineer for the KC-390 Flight Management System and GNSS. Currently, he has joined Pilatus Aircraft Ltd. as an Avionics System Engineer to work with the navigation and communication systems of the PC-12 and PC-24 aircraft. His research interests include the effects of the ionosphere on the global navigation satellite system (GNSS) signal under low latitudes.

Alison Moraes received the B.S. degree in telecommunications engineering from the Universidade de Taubaté, São Paulo, Brazil, in 2003, and the M.S. and Dr.Sc. degrees in electronic and computer engineering from the Aeronautics Institute of Technology (ITA), São José dos Campos, Brazil, in 2009 and 2013, respectively.

He has been a Technologist with the Aeronautics and Space Institute, since 2004, and a Graduate Professor with ITA, since 2015. He has authored more than 40 articles. His research interests include statistical models for ionospheric radio signals, low-cost platforms for science dissemination, avionics, and space systems engineering.

Dr. Moraes is currently an Associate Editor for the *Journal of Aerospace Technology and Management*.

Jonas Sousasantos received the graduate degree in mathematics from the Universidade de Taubaté, State of São Paulo, Brazil, in 2010, and the M.Sc. and Ph.D. degrees in space geophysics from the Instituto Nacional de Pesquisas Espaciais, São José dos Campos, Brazil, in 2013 and 2017, respectively.

He is currently engaged with the Scintillation Prediction Observations Research Task project as a Postdoctoral Researcher.

Leonardo Marini-Pereira received the B.S. degree in cartography engineering from the University of São Paulo State, Presidente Prudente, São Paulo, Brazil, in 2005, and the M.S. degree in remote sensing and geoprocessing from the National Institute for Space Researches, São José dos Campos, Brazil, in 2008. He is currently working toward the Ph.D. degree in space science and technology at the Aeronautics Institute of Technology, São José dos Campos, Brazil.

He has been in the military of the Brazilian Air Force, currently at the rank of Major, working with the Department of Airspace Control, since 2007.

Sam Pullen was born in San Antonio, TX, USA, in 1966. He received two S.B. degrees in aeronautics and astronautics and history from the Massachusetts Institute of Technology, Cambridge, MA, USA, in 1989, and the M.S. and Ph.D. degrees in aeronautics and astronautics from Stanford University, Stanford, CA, USA, in 1990 and 1996, respectively.

Since receiving the Ph.D. degree, he has been a Researcher (currently, Senior Research Engineer, part-time) with the GPS/GNSS Laboratory, Aeronautics and Astronautics Department, Stanford University. He also supports government, industry, and legal clients as a Technical Consultant. He has authored several book chapters and more than 150 articles. His research interests include system integrity assurance and design optimization under uncertainty, especially for users of global satellite navigation systems and enhancements such as ground and satellite-based augmentation systems.

Dr. Pullen was an Associate Editor of the journal *IEEE TRANSACTIONS ON AEROSPACE AND ELECTRONIC SYSTEMS* from 2007 to 2015 and holds one patent. He was a recipient of the Institute of Navigation (ION) Early Achievement Award in 1999 and became a Fellow of the ION in 2017.